#### 九州大学学術情報リポジトリ Kyushu University Institutional Repository

# Stacking Faults and Intercalants in (Ta\_<1-x>Ti\_x)Se\_2 Revealed by Cross-Sectional Transmission Electron Microscopy

Sato, Kazuhisa

Research Center for Ultra-High Voltage Electron Microscopy, Osaka University

Matsushita, Toshiya

Research Center for Ultra-High Voltage Electron Microscopy, Osaka University

https://hdl.handle.net/2324/7393031

出版情報: The Journal of Physical Chemistry C. 126 (33), pp.14290-14296, 2022-08-11. American Chemical Society (ACS)

バージョン:

権利関係: This document is the Accepted Manuscript version of a Published Work that appeared in final form in The Journal of Physical Chemistry C, copyright © 2022 American Chemical Society after peer review and technical editing by the publisher. To access the final edited and published work see "関連DOI(Related DOI)".



## Stacking faults and intercalants in $(Ta_{1-x}Ti_x)Se_2$ revealed by cross-sectional transmission electron microscopy

Kazuhisa Sato\* and Toshiya Matsushita

Research Center for Ultra-High Voltage Electron Microscopy, Osaka University, 7-1 Mihogaoka,

Ibaraki, 567-0047, Japan

<sup>\*</sup>Corresponding author. sato@uhvem.osaka-u.ac.jp

**ABSTRACT**: Structural defects in layered compounds  $(Ta_{1-x}Ti_x)Se_2$   $(0 \le x \le 1)$ , characterized by anisotropy in electrical conductivity, have been studied by cross-sectional observation using chemically sensitive high-angle annular dark-field scanning transmission electron microscopy (HAADF-STEM). Intercalants were detected in the widest space between Se atoms across the van der Waals (vdW) gap, regardless of the Ti content (except TiSe<sub>2</sub>) or thermal history after the crystal growth. Binary TaSe<sub>2</sub> both 3R and 2H structures include high density stacking faults, while the Ti addition stabilize 1T structure with no stacking faults. We show that chemical composition dominates the structural defects in the  $(Ta_{1-x}Ti_x)Se_2$  compounds. Substitution of Ta by Ti acts as a hole addition, which reduces the number of conduction electrons in the layer, while an intercalated atom in the vdW gap may not act as a donor of conduction electrons.

#### INTRODUCTION

Transition metal dichalcogenides (TMDCs) are layered compounds that form a charge density wave (CDW) due to Peierls instability<sup>1</sup>. The CDW phase transition generates periodic lattice distortion (PLD) induced by the electron-phonon interaction. The wave vector of a CDW depends on the shape of the Fermi surface. These features stabilize a long-period superstructure (LPS) within the layer. The structural feature of the TMDCs is the formation of several polytypes with different atomic layer stacking. For example, TaSe2, which is one of the typical TMDCs characterized by anisotropy in electrical conductivity, forms polytypes such as 1T, 2H, 3R, and  $4H_b^{2-5}$ . Each polytype shows different CDW phases with definite transition temperatures<sup>2</sup>. Constituent atoms are covalently bonded within the structural units, while the stacked layers are bonded via the van der Waals (vdW) force. Such a unique chemical bonding leads to anisotropy in electrical conductivity; renewed attention has been paid for nanoelectronics application of TMDCs <sup>6, 7</sup>. Electronic states can be tuned by substituting host metals. For example, in TaSe<sub>2</sub>, substitution of Ta with Ti changes the LPS as well as the electronic structure<sup>8</sup>. However, substitution sites and possible intercalants in the vdW gap still remain an open question.

To date, in-plane atomic structures of the CDW phases in TMDCs have been characterized using scanning tunneling microscopy (STM)<sup>9</sup> and transmission electron microscopy (TEM)<sup>10, 11</sup>. However, few report exists on structural characterization of the cross-section of the layered structure. Weak interlayer bonding via the vdW force may prevent sample preparation of a cross-section. Recently, we have

achieved cross-sectional microsampling of a flake-like TMDC single crystal using the focused ion-beam (FIB) technique.

Current structural characterization of the TMDCs have largely relied on high-angle annular dark-field scanning transmission electron microscopy (HAADF-STEM) with an improved resolution and chemical sensitivity known as atomic number contrast (Z-contrast). The latest imaging techniques enable atomic scale characterization of structural and chemical irregularities in the CDW phases<sup>12-14</sup>. The purpose of this study is to clarify the structural defects in the  $(Ta_{1-x}Ti_x)Se_2$  ( $0 \le x \le 1$ ) by means of cross-sectional HAADF-STEM observation with atomic-scale resolution. We compared the atomic structures of both quenched and furnace cooled  $(Ta_{1-x}Ti_x)Se_2$  crystals as a function of Ti content.

#### **MATERIALS AND METHODS**

Sample Preparation. ( $Ta_{1-x}Ti_x$ )Se<sub>2</sub> crystals ( $0 \le x \le 1$ ) were prepared by the chemical vapor transport (CVT) method. The process was composed of the following two steps. First, mixed powder of Ta, Ti, Se was vacuum encapsulated in a quartz tube ( $\sim 10^{-4}$  Pa) and then annealed at 1223 K for 170 h, followed by furnace cooling<sup>12</sup>. Subsequently, iodine ( $I_2$ ) powder was added to the annealed powder as a transport agent for the CVT process, and again sealed in a quartz tube. The targeted crystals were grown over 170 h under a temperature gradient of 1223 K and 1023 K. After the crystal growth, the quartz tube was furnace-cooled (about 12 hours for cooling to the room temperature) or quenched in ice water without breaking the tube. We obtained flake-shaped single crystal pieces with a maximum

size of about 2 mm. Plan-view TEM specimens were prepared by cleaving crystals using scotch tape. Cross-sectional TEM specimens were prepared using a focused ion beam (FIB) instrument (Thermo Fisher Scientific Scios2 Dual Beam) with Ga ions. The thinning was first processed with an energy of 30 keV and finished with 2 keV.

Characterization. The structure and morphology of the prepared specimens were characterized using a JEOL JEM- ARM200F TEM operating at 200 kV with a CEOS aberration corrector for the probe-forming lens. For STEM imaging, we set the beam convergence to 23 mrad in semiangle, and HAADF-STEM images were acquired with detector semiangles of 68–170 mrad. Thickness of TEM specimens were estimated by electron-energy loss spectroscopy (EELS) using a post-column energy filter (Gatan Quantum ER). Compositional analyses were performed using an energy-dispersive x-ray spectrometer (EDS; JEOL JED-2300). Chemical composition was determined by TEM-EDS based on the thin film approximation. Accuracy of the EDS analysis was estimated to be 1–2% in statistical error of the integrated intensity of the characteristic x-ray. STEM images were simulated using the STEMSLIC code<sup>24</sup> and the TEMPAS (Total Resolution LLC).

#### **RESULTS AND DISCUSSION**

Figure 1 shows schematic illustrations of the three kinds of polytypes deal with in this study; (a) 3R, (b) 2H, and (c) 1T. Here, the lattice type of 3R and 1T are trigonal, while 2H is hexagonal. All these models are viewed in the  $\lceil 11\bar{2}0 \rceil$  direction. The Se-layer is coordinated above and below the Ta-layer

to form a structural unit, and these are laminated in the [0001] direction. Each structural unit is connected at the (0001) atomic plane by vdW force, and the space between layers is termed as the vdW gap. According to the notation reported by Katzke et al.<sup>15</sup>, stacking sequences can be represented as follows: (a) 3*R*: *AbA BcB CaC*, (b) 2*H*: *AbA CbC*, (c) 1*T*: *CbA* where capital letters correspond to the chalcogen (Se) positions and lower case letters show the metal (Ta) positions.

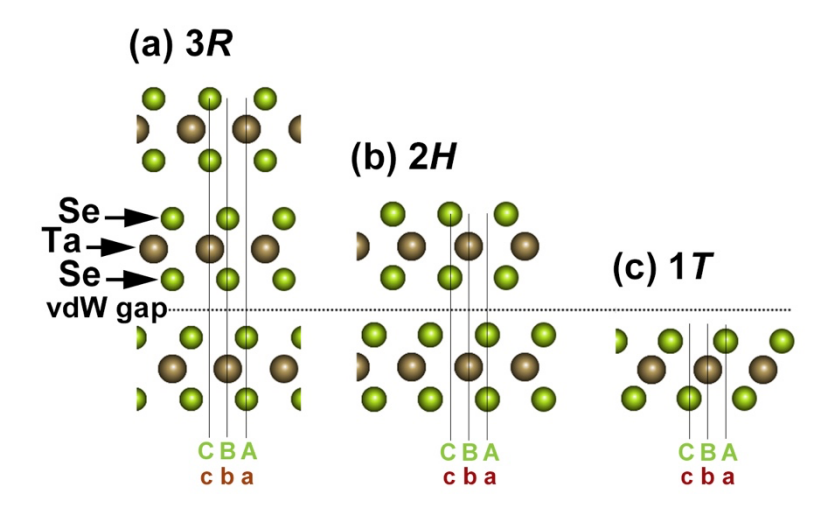


**Figure 1**. Schematic illustrations of the three kinds of polytypes deal with in this study; (a) 3R, (b) 2H, and (c) 1T viewed in the  $[11\overline{2}0]$  direction.

Figure 2(a) shows a cross-sectional HAADF-STEM image of the quenched TaSe<sub>2</sub>. The structural unit consists of one bright atom and two slightly dark atoms, and the vdW gap between the structural units is observed with dark contrast. From the analysis of the selected area electron diffraction (SAED) pattern shown in the upper inset, it was found that the crystal structure is the 3R-type. The beam incidence is in the [11 $\overline{2}$ 0] direction. Atomic positions are arranged in a zigzag in the [0001] direction;

namely along the c-axis. A simulated image shown in the lower inset is qualitatively consistent with the observed one. Stacking faults are also seen where the zigzag is reversed as indicated by arrowheads, e.g., AbA BcB CaC | BaB AcA CbC (stacking fault is denoted by |). Weak streaks extending in the caxis direction of the SAED pattern indicate the high-density distribution of the stacking faults perpendicular to the c-axis. Z contrast of the HAADF-STEM is proportional to the  $\alpha$  th power of the atomic number ( $Z^{\alpha}$ ,  $\alpha$ : the exponent close to 2 based on the Rutherford scattering) of the constituent elements  $^{16}$ . Therefore, the brightest atoms and the slightly darker atoms can be assigned Ta (Z = 73) and Se (Z = 34), respectively. A simulated image shown in the lower inset is qualitatively consistent with the observed one. Noticeable feature is that there are contrasts in vdW gaps as marked by circles. These contrasts can be attributed to interlayer atoms; namely, intercalants, either Ta or Se, or both. Figure 2(b) shows a cross-sectional HAADF-STEM image of the quenched  $(Ta_{1-x}Ti_x)Se_2$  ( $x \sim 0.24$ ). The crystal structure is the 1T-type. The beam incidence is in the  $[11\bar{2}0]$  direction. A simulated image shown in the lower inset is qualitatively consistent with the observed one. Corresponding SAED

The crystal structure is the 1T-type. The beam incidence is in the  $[11\bar{2}0]$  direction. A simulated image shown in the lower inset is qualitatively consistent with the observed one. Corresponding SAED pattern include no streak, and in fact stacking faults were not observed in this specimen. However, contrasts by intercalants are also observed in the vdW gaps as marked by circles. It should be mentioned that each polytype looks alike when observed in the  $[1\bar{1}00]$  direction (Figure S1).

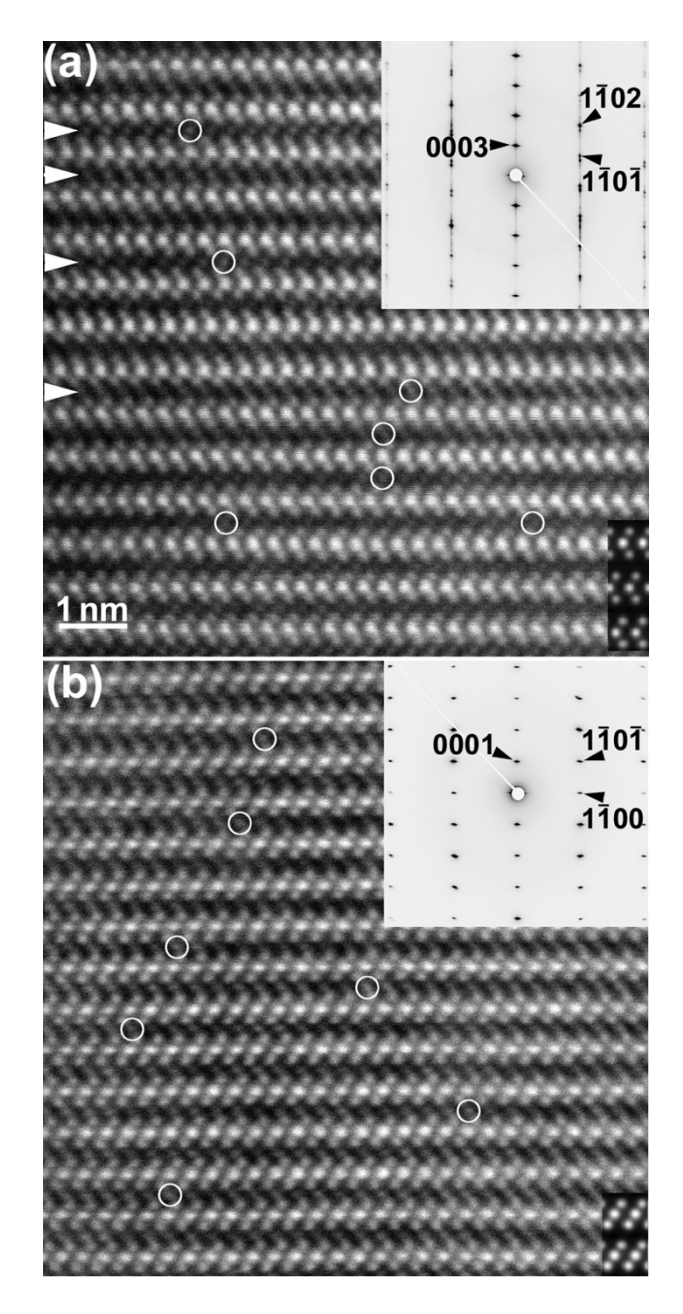
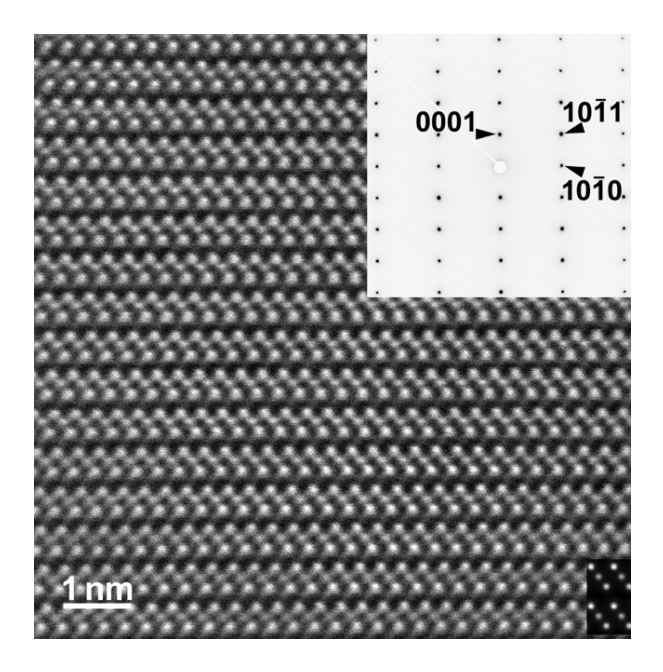


Figure 2. (a) A cross-sectional HAADF-STEM image of the quenched 3R-TaSe<sub>2</sub> observed in the [11 $\overline{2}$ 0] direction. (b) A cross-sectional HAADF-STEM image of the quenched 1T-(Ta<sub>1-x</sub>Ti<sub>x</sub>)Se<sub>2</sub> ( $x \sim 0.24$ ) observed in the [11 $\overline{2}$ 0] direction. An SAED pattern (upper inset) and a simulated STEM image (lower inset) are also shown in each image.

Figure 3 shows a cross-sectional HAADF-STEM image of the furnace cooled TiSe<sub>2</sub>. Corresponding

SAED pattern is shown in the upper inset. The crystal structure is the 1T-type. The beam incidence is in the  $[\bar{1}2\bar{1}0]$  direction. A simulated image shown in the lower inset is qualitatively consistent with the observed one. As seen, the stacking of Se-Ti-Se is AbC, which is different from that shown in Fig. 2(b) (CbA) with the  $[11\bar{2}0]$  direction. A noticeable feature of this specimen is that there is no intercalant in the vdW gaps; both Ti and Se atoms tend not to replace the interlayer sites. In fact, existence of a very small number of intercalated-Ti atoms  $(4.8\times10^{-2} \text{ atoms/nm}^{-2})$  has been reported in 1T-TiSe<sub>2</sub> using scanning tunneling microscopy<sup>17</sup>. This result implies that the large number of contrasts observed in the vdW gaps of the TaSe<sub>2</sub> (Fig.2(a)) and  $(Ta_{1-x}Ti_x)Se_2$  ( $x \sim 0.24$ ) (Fig. 2(b)) are likely to be Ta atoms.



**Figure 3**. A cross-sectional HAADF-STEM image of the furnace cooled 1T-TiSe<sub>2</sub> observed in the  $[\overline{1}2\overline{1}0]$  direction. An SAED pattern (upper inset) and a simulated STEM image (lower inset) are also shown.

Figure 4(a) shows a cross-sectional HAADF-STEM image of the furnace cooled TaSe<sub>2</sub>. The crystal structure is the 2H-type. The beam incidence is in the [ $11\overline{2}0$ ] direction. A simulated image shown in the lower inset is qualitatively consistent with the observed one. Intercalants are also observed in the vdW gaps as marked by circles. Streaks appear in the SAED pattern and stacking faults are observed in the HAADF-STEM image as indicated by arrowheads. This result revealed that origin of the stacking faults is not due to the thermal history; namely, rapid quenching or slow cooling after the crystal growth.

Figure 4(b) shows a cross-sectional HAADF-STEM image of the furnace cooled  $(Ta_{1-x}Ti_x)Se_2$  ( $x \sim 0.24$ ). The crystal structure is the 1*T*-type. The beam incidence is in the [11 $\overline{2}0$ ] direction. A simulated image shown in the lower inset is qualitatively consistent with the observed one. Intercalants are also observed in the vdW gaps as marked by circles. Similarly, the 1*T*-structure was obtained for a specimen with  $x \sim 0.36$  (Figure S2). Thus, the addition of Ti seems to stabilize the 1*T* structure, which is the structure of TiSe<sub>2</sub>.

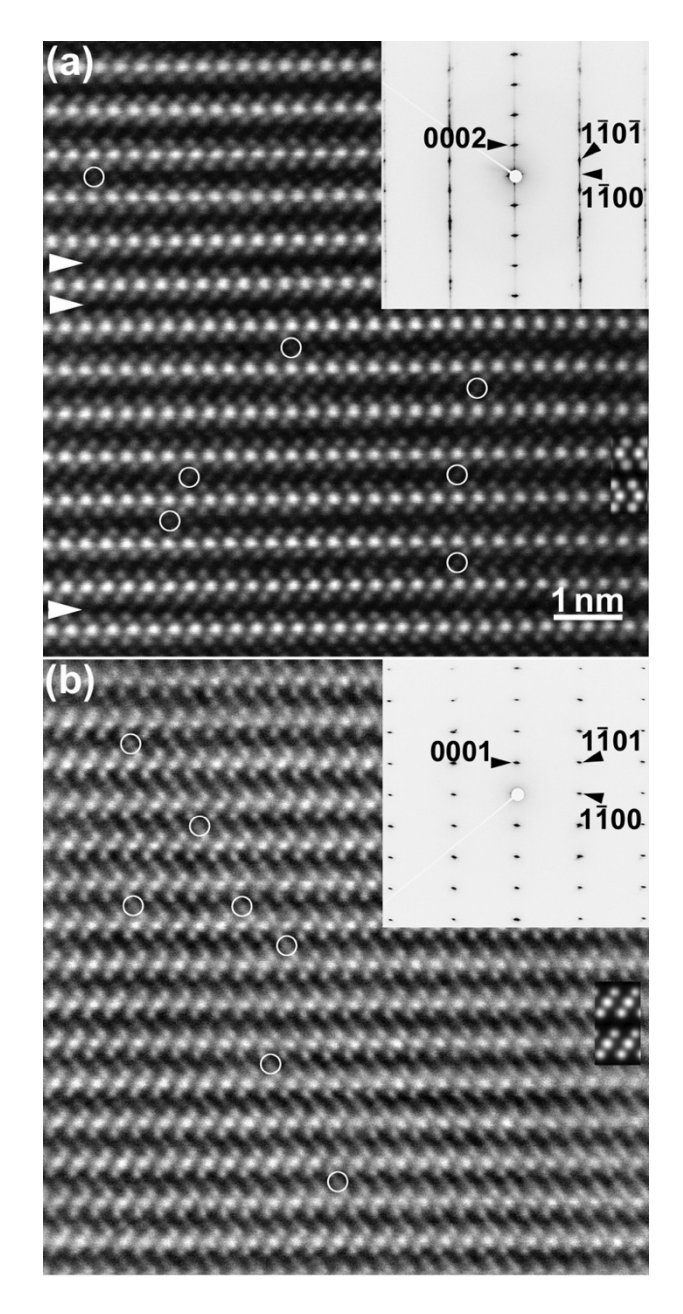


Figure 4. (a) A cross-sectional HAADF-STEM image of the furnace cooled 2H-TaSe<sub>2</sub> observed in the [11 $\overline{2}$ 0] direction. (b) A cross-sectional HAADF-STEM image of the furnace cooled 1T-(Ta<sub>1-x</sub>Ti<sub>x</sub>)Se<sub>2</sub> ( $x \sim 0.24$ ) observed in the [11 $\overline{2}$ 0] direction. An SAED pattern (upper inset) and a simulated STEM image (lower inset) are also shown in each image.

As shown in Figs. 2-4, existence of the intercalants were found for the (Ta<sub>1-x</sub>Ti<sub>x</sub>)Se<sub>2</sub> specimens

except x = 1 (TiSe<sub>2</sub>), while the stacking faults were observed for specimens with x = 0 (TaSe<sub>2</sub>). These features are independent of the thermal history after the crystal growth. Thus, chemical composition dominates the structural defects in the  $(Ta_{1-x}Ti_x)Se_2$  compounds. Based on the atomic image analyses, it was found that the interlayer atoms locate in the widest space (interatomic distance of  $\sim 0.38$  nm) between the Se atoms facing each other across the vdW gap as indicated by arrows in Fig. 5. This tendency has been experimentally verified in this study regardless of the polytypes. Dotted lines indicate the position of the stacking faults experimentally observed.

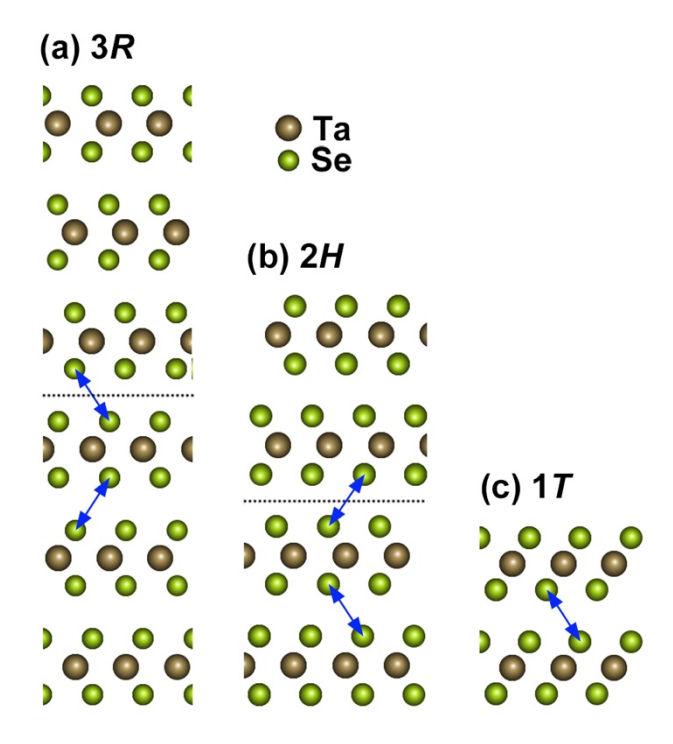
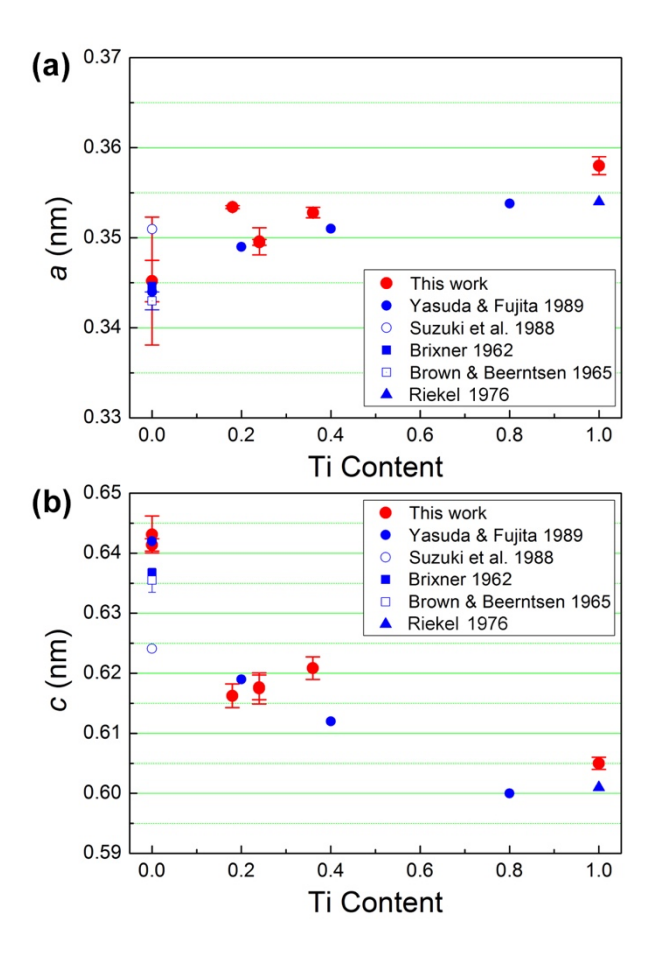


Figure 5. Schematic illustrations of the three kinds of polytypes indicating the widest space (interatomic distance of  $\sim 0.38$  nm) between the Se atoms facing each other across the vdW gap (arrows) and the location of the stacking fault. (a) 3R, (b) 2H, and (c) 1T viewed in the [ $11\overline{2}0$ ] direction.

Figure 6(a) and 6(b) show, respectively, Ti-content dependence of the lattice parameters, a and c.

Note that for the 3R and the 2H structures, c/3 and c/2 are plotted, respectively. The lattice parameters were measured from the SAED patterns using a Au-Pd thin film mounted on a Cu grid as "standard" for the camera-length correction in SAED. The standard deviation was calculated using the measured lattice parameters assuming a Gaussian distribution. As the Ti content increases, the a-axis stretched and the c-axis shrunk. The tendency is consistent with that reported in the literature  $^{18-22}$ . The lattice parameters of the  $(Ta_{1-x}Ti_x)Se_2$  change toward the value for the  $TiSe_2$  as the Ti-content increases. Intercalation may induce lattice distortion as indicated by Hildebrand et al.  $^{23}$ , while the experimental results suggest that the lattice parameters seem to be rather independent of the presence of intercalants or anti-site atoms. It is presumed that the intercalants or anti-site atoms are randomly distributed and their number are not large enough to affect lattice parameters.



**Figure 6**. (a) Ti-content dependence of the lattice parameter, a. (b) Ti-content dependence of the lattice parameter, c. For the 3R and the 2H structures, c/3 and c/2 are plotted, respectively.

To clarify the structural defects such as anti-site atoms, we analyzed the intensity of the atomic position of the HAADF-STEM images. Figure 7(a) shows Ti content dependence of the intensity of bright spots of Ta atom sites and intercalant sites both normalized by that of the Se atom sites for the quenched specimens observed in the  $[11\overline{2}0]$  direction. The intensities were measured at a region including the bright spots of Ta, Se, or interlayer atoms (each intensity is defined as sum of the intensities of  $15 \times 15$  pixels per atomic position). As the Ti-content increased, intensity of the Ta-atom sites decreased by 15%, while the intercalant sites increased by 40%. The decrease in image intensity

of the Ta-site can be explained by the consequence of substitution of Ta (Z = 73) with the lighter Ti (Z = 22); namely, anti-site atoms. In contrast, the increase in image intensity of the intercalant sites can be affected by multiple factors such as (1) an increase in the number of intercalants, (2) depth of the position of the intercalants in the electron propagation direction, (3) an increase in heavy Ta atoms located at the vdW gap, or (4) superposition of these effects. We estimated the specimen thickness to be around 30–40 nm using the electron energy loss spectroscopy; approximately 90–120 atoms exist along an atomic column in the electron propagation direction. Hence it is difficult to identify the cause; however, it is inferred that some of Ta atoms replaced with Ti may be ejected to the vdW gap between the layers during the crystal growth.

The results obtained for the furnace cooled specimens are shown in Fig. 7(b). Overall feature is qualitatively similar to those of the quenched specimens. We also examined the HAADF-STEM image intensity obtained in the [ $1\bar{1}00$ ] direction. Results for quenched and furnace cooled specimens are shown in Fig. 7(c) and 7(d), respectively. Almost the same results as in the case of the [ $11\bar{2}0$ ] incidence were obtained. Thus, we can conclude that intensity of the Ta-atom sites decrease, and the intercalant sites increase as the Ti-content increases in  $(Ta_{1-x}Ti_x)Se_2$  compounds.

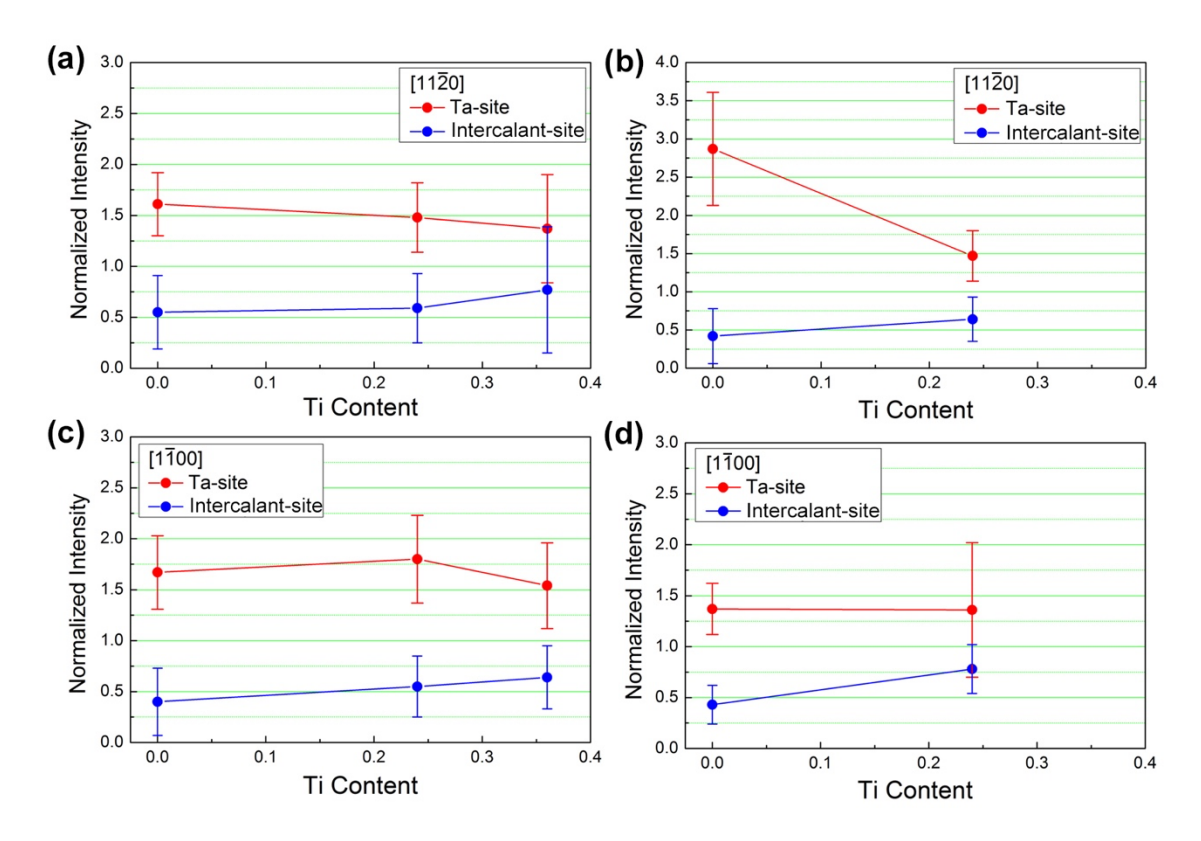


**Figure 7**. Ti content dependence of the intensity of the bright spots of Ta atom sites and intercalant sites both normalized by that of the Se atom sites. for the quenched specimens observed in the  $[11\bar{2}0]$  direction. (a) quenched, beam //  $[11\bar{2}0]$ , (b) furnace cooled, beam //  $[11\bar{2}0]$ , (c) quenched, beam //  $[1\bar{1}00]$ , (d) furnace cooled, beam //  $[1\bar{1}00]$ .

Substitution of Ta  $(5d^36s^2)$  by Ti  $(3d^24s^2)$  acts as a hole addition, which reduces the number of conduction electrons in the layer and shrinks the Fermi surface. To verify this scenario, we observed SAED patterns in plan-view geometry with [0001] zone. Figures 8(a), (b), and (c) show, respectively, the SAED patterns obtained for the quenched specimens with Ti content of x = 0, 0.24, and 0.3. Satellite reflections due to the CDW phase were observed around the fundamental reflections as shown in Figs. 8(a)-(c). In Figs. 8 (b) and 8 (c), magnified images of one fundamental reflection and surrounding

weak satellite reflections are shown in the lower insets. The crystal structures of these three specimens are all 1*T*-type (Note that 3*R* structure was also obtained in the quenched TaSe<sub>2</sub> as shown in Fig.2(a)). We measured the values  $|q|/|a^*|$  where q and  $a^*$  denote reciprocal lattice vectors of the satellite reflections and the fundamental ones, respectively. The example of q and  $a^*$  are indicated in Fig. 8(d). The obtained Ti content dependence of the  $|q|/|a^*|$  (Figure 8(e)) revealed that the ratio decreases as the Ti content increases; that is, q decreases faster than  $a^*$  with respect to the Ti content. The wave vector q is determined by the shape of the Fermi surface<sup>2, 3</sup>, which is affected by the number of conduction electrons. Namely, the number of conduction electrons are reduced by increasing Ti content in the layer, which results in the reduction of the q vector of the CDW phase. This tendency is consistent with the previous study by Wilson et al.<sup>3</sup> Thus, Fig. 8(e) clearly indicates the decrease of conduction electrons induced by substitution of Ta by Ti. In this study, we found numerous intercalants in the vdW gaps of the  $(Ta_{1-x}Ti_x)Se_2$  except for the  $TiSe_2$  (x = 1). It is presumed that an intercalated atom in the vdW gap may not act as a donor of conduction electrons. In another study on 1T-TiSe<sub>2</sub>, a diminution of the CDW domain size by Ti self-doping has been reported<sup>17</sup>, and hence the presently observed intercalants in the vdW gap may also inhibit the CDW of the (Ta<sub>1-x</sub>Ti<sub>x</sub>)Se<sub>2</sub>.

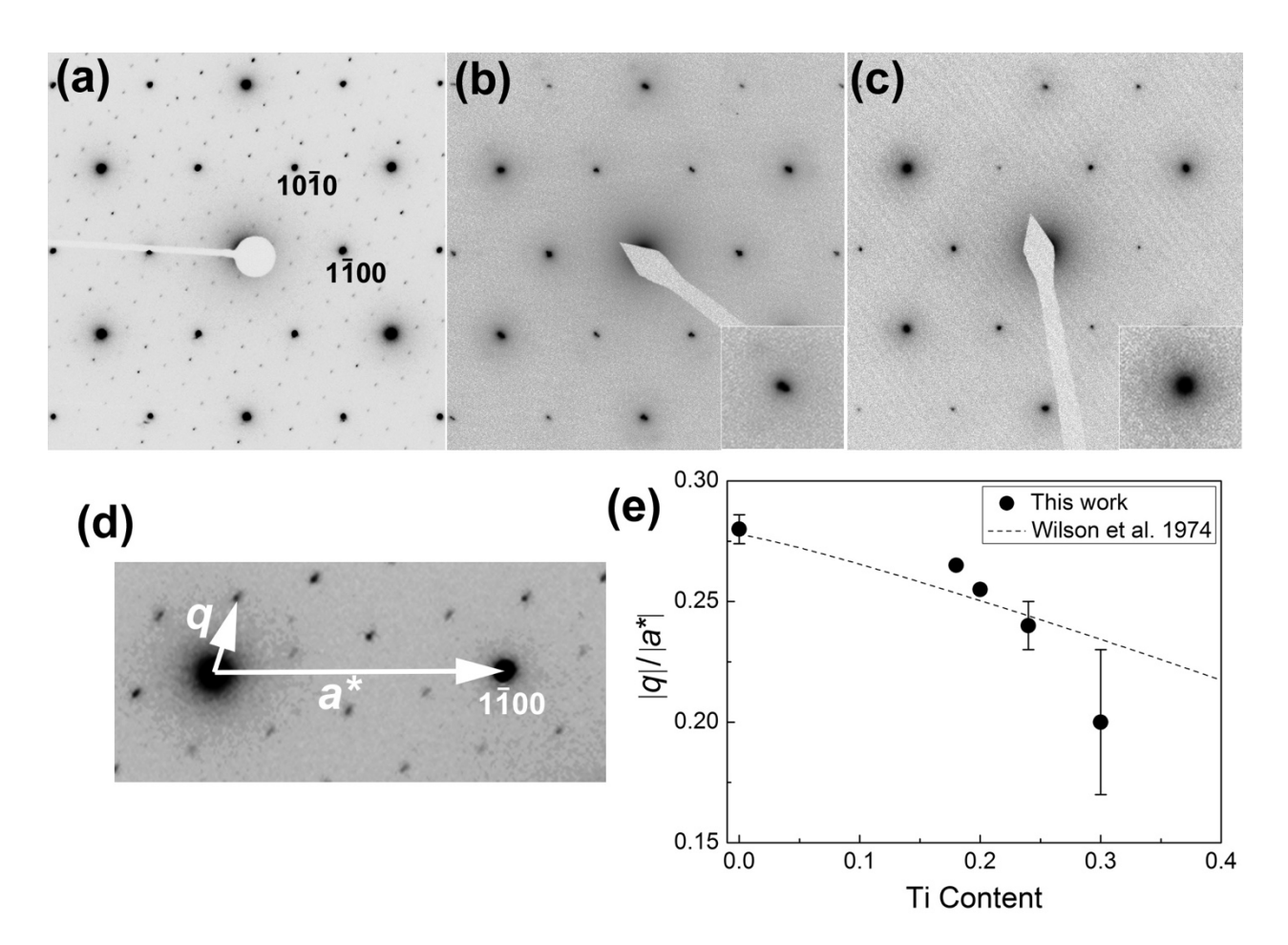


**Figure 8**. SAED patterns obtained for the quenched (a) TaSe<sub>2</sub>, (b)  $(Ta_{1-x}Ti_x)Se_2$  ( $x \sim 0.24$ ), and (c)  $(Ta_{1-x}Ti_x)Se_2$  ( $x \sim 0.3$ ) observed in the [0001] direction. (d) A magnified image of the pattern shown in Fig.8(a), indicating the q and  $a^*$ . (e) Ti-content dependence of the value  $|q|/|a^*|$ .

#### **CONCLUSIONS**

In conclusion, we have directly shown the existence of intercalants in the vdW gap of  $(Ta_{1-x}Ti_x)Se_2$ . The intercalants are judged to be Ta atoms rather than Ti or Se atoms. Thermal history after the crystal growth such as quenching or slow cooling little affects the structural defects. The intercalants exist in the widest space between the Se atoms across the vdW gap. The 3R and the 2H-type  $TaSe_2$  include high density stacking faults, while the Ti addition stabilizes the 1T structure with no stacking faults.

We show that chemical composition dominates the structural defects in the  $(Ta_{1-x}Ti_x)Se_2$ . Substitution of Ta by Ti acts as a hole addition, which reduces the number of conduction electrons in the layer, while an intercalated Ta atom may not act as a donor of conduction electrons. This finding will be useful for applications of the layered compounds such as TMDCs to nanoelectronics. Further study is needed to elucidate the origin of intercalants formation.

#### **ASSOCIATED CONTENT**

#### **Supporting Information**

The Supporting Information is available free of charge at

https://

Additional HAADF-STEM images (PDF)

#### **AUTHOR INFORMATION**

#### **Corresponding Author**

Kazuhisa Sato -Research Center for Ultra-High Voltage Electron Microscopy, Osaka University,

Ibaraki, 5670047, Japan; orcid/org/0000-0001-9078-2541; Email: sato@uhvem.osaka-u.ac.jp

\*E-mail: sato@uhvem.osaka-u.ac.jp

#### **Author**

Toshiya Matsuhista – Research Center for Ultra-High Voltage Electron Microscopy, Osaka University,

Ibaraki, 5670047, Japan

#### **Author Contributions**

All authors contributed to the discussion and writing of the manuscript. The final version of the manuscript was approved by all authors.

#### **Notes**

The authors declare no competing financial interest.

#### **ACKNOWLEDGMENTS**

This study was partially supported by the program Advanced Research Network for Ultra-Microscopic Science (FY2016–2021) from the Ministry of Education, Culture, Sports, Science, and Technology (MEXT), Japan and the JSPS KAKENHI (Grant Nos. 21H01764 and 20K21129). The authors would like to express their sincere gratitude to Dr. H. Yasuda and Mr. R. Nakamura for their helps in this study.

#### **REFERENCES**

- (1) Peierls, R. E. Quantum Theory of Solids; Oxford University Press: Oxford, 1955.
- (2) Wilson, J. A.; Di Salvo, F. J.; Mahajan, S. Charge-density waves and superlattices in the metallic layered transition metal dichalcogenides. *Adv. Phys.* **1975**, *24*, 117–201.
- (3) Wilson, J. A.; Di Salvo; F. J., Mahajan, S. Charge-density waves in metallic, layered, transition-metal dichalcogenides. *Phys. Rev. Lett.* **1974**, *32*, 882–885.
- (4) Brown, B. E.; Beerntsen, D. J. Layer structure polytypism among niobium and tantalum selenides. *Acta Cryst.* **1965**, *18*, 31–36.
- (5) Moret, R.; Tronc, E. Atomic displacements in the charge-density wave induced superstructure of 4H<sub>b</sub>-TaSe<sub>2</sub>. *Phil. Mag. B* **1979**, *40*, 305–315.
- (6) Neal, A. T.; Du, Y.; Liu, H.; Ye, P. D. Two-dimensional TaSe<sub>2</sub> metallic crystals: spin-orbit scattering length and breakdown current density. *ACS Nano* **2014**, *8*, 9137–9142.
- (7) Tsoutsou, D.; Aretouli, K. E.; Tsipas, P.; Marquez-Velasco, J.; Xenogiannopoulou, E.; Kelaidis, N.; Giamini, S. A.; and Dimoulas, A. Epitaxial 2D MoSe<sub>2</sub> (HfSe<sub>2</sub>) semiconductor/2D TaSe<sub>2</sub> metal van der Waals heterostructures. *ACS Appl. Mater. Interfaces* **2016**, *8*, 1836–1841.
- (8) Di Salvo, F. J.; Wilson, J. A.; Bagley, B. G.; Waszczak, J. V. Effects of doping on charge-density waves in layer compounds, *Phys. Rev. B* **1975**, *12*, 2220–2235.
- (9) Wu, X. L.; Lieber, C. M. Direct characterization of charge-density-wave defects in titanium-doped TaSe<sub>2</sub> by scanning tunneling microscopy. *Phys. Rev. B* **1990**, *41*, 1239–1242.

- (10) Ishiguro, T.; Sato, H. Electron microscopy of phase transformations in 1T-TaS<sub>2</sub>. *Phys. Rev. B* **1991**, 44, 2046–2060.
- (11) Börner, P. C.; Kinyanjui, M. K.; Björkman, T.; Lehnert, T.; Krasheninnikov, A. V.; Kaiser, U. Observation of charge density waves in free-standing 1T-TaSe<sub>2</sub> monolayers by transmission electron microscopy. *Appl. Phys. Lett.* **2018**, *113*, 173103.
- (12) Kobayashi, K.; Yasuda H. Direct visualization of the periodic displacement of Ta atoms in the commensurate charge density wave phase of 1*T*-TaSe<sub>2</sub> in real space. *Phys. Rev. B* 2016, *94*, 201409(R).
  (13) Kobayashi, K.; Yasuda H. Formation of superstructure in 1*T*-TiSe<sub>2</sub> induced at room temperature
- by electron beam irradiation. *Mat. Res. Exp.* **2018**, *5*, 085006.
- (14) Kobayashi, K.; Yasuda H. Formation mechanism of  $2a \times 2a$  long-range ordered structure in 1*T*-TiSe<sub>2</sub> induced by electron beam irradiation and its spontaneous enlargement. *Chem. Phys. Lett.* **2020**, 759, 137953.
- (15) Katzke, H.; Tolédano, P.; Depmeier, W. Phase transitions between polytypes and intralayer superstructures in transition metal dichalcogenides. *Phys. Rev. B* **2004**, *69*, 134111.
- (16) Jesson, D. E.; Pennycook, S. J. Incoherent imaging of crystals using thermally scattered electrons. *Proc. R. Soc. Lond. A* **1995**, *449*, 273–293.
- (17) Hildebrand, B.; Jaouen, T.; Didiot, C.; Razzoli, E.; Monney, G.; Mottas, M.-L.; Ubaldini, A.; Berger, H.; Barreteau, C.; Beck, H.; Bowler, D. R.; Aebi, P. Short-range phase coherence and origin of the 1T-TiSe<sub>2</sub> charge density wave. *Phys. Rev. B* **2016**, *93*, 125140.

- (18) Yasuda, H.; Fujita, H. Electron state of solute atom and lattice distortion in two-dimensional metals (Ta<sub>1-x</sub>Ti<sub>x</sub>)Se<sub>2</sub>. *J. Japan Inst. Metals.* **1989**, *53*, 1191–1197.
- (19) Suzuki, A.; Yamashita, T.; Matsui, K.; Doyama, M. Thermal and structural measurements of the mixed crystals 1T-TaS<sub>2-x</sub>Se<sub>x</sub>. *J. Phys. Soc. Jpn.* **1988**, *57*, 1707–1716.
- (20) Brixner, L. H.; Preparation and properties of the single crystalline AB<sub>2</sub>-type selenides and tellurides of niobium, tantalum, molybdenum and tungsten. *J. Inorg. Nucl. Chem.* **1963**, *24*, 257–263.
- (21) Brown, B. E.; Beerntsen, D. J. Layer structure polytypism among niobium and tantalum selenides. *Acta Cryst.* **1965**, *18*, 31–36.
- (22) Riekel, C. Structure refinement of TiSe<sub>2</sub> by neutron diffraction. *J. Solid State Chem.* **1976**, *17*, 389–392.
- (23) Hildebrand, B.; Jaouen, T.; Didiot, C.; Razzoli, E.; Monney, G.; Mottas, M. -L.; Vanini, F.; Barreteau, C.; Ubaldini, A.; Giannini, E.; Berger, H.; Bowler, D. R.; Aebi, P. Local resilience of the 1*T*-TiSe<sub>2</sub> charge density wave to Ti self-doping. *Phys. Rev. B* **2017**, *95*, 081104(R).
- (24) Kirkland, E. J. Advanced computing in electron microscopy; Plenum Press: NY, 1998.

#### **Supporting Information**

### Stacking Faults and Intercalants in (Ta<sub>1-x</sub>Ti<sub>x</sub>)Se<sub>2</sub> Revealed by Cross-Sectional Transmission Electron Microscopy

Kazuhisa Sato\* and Toshiya Matsushita

Research Center for Ultra-High Voltage Electron Microscopy, Osaka University, 7-1 Mihogaoka, Ibaraki, 567-0047, Japan

Corresponding author.

\*E-mail: sato@uhvem.osaka-u.ac.jp

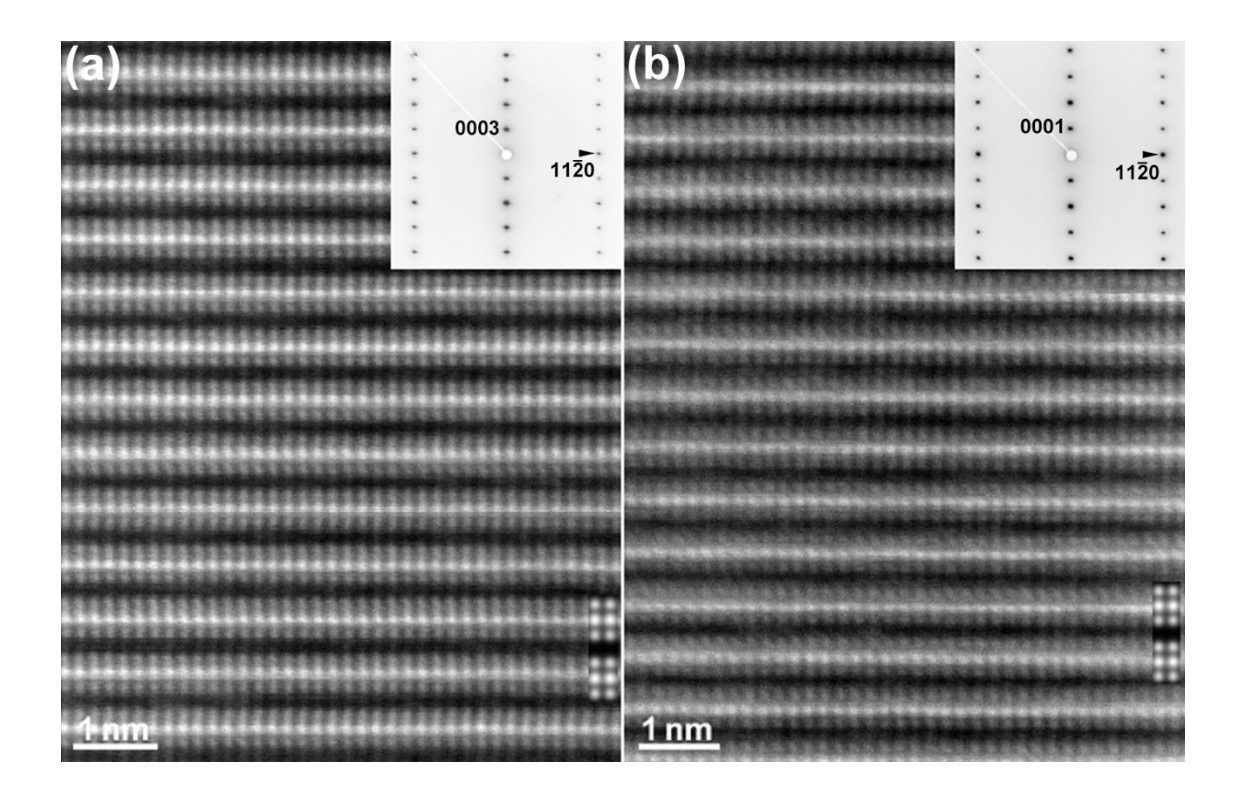


**Figure S1**. (a) A cross-sectional HAADF-STEM image of the quenched 3R-TaSe<sub>2</sub> observed in the [1 $\bar{1}$ 00] direction. (b) A cross-sectional HAADF-STEM image of the quenched 1T-(Ta<sub>1-x</sub>Ti<sub>x</sub>)Se<sub>2</sub> (x~0.24) observed in the [1 $\bar{1}$ 00] direction. An SAED pattern (upper inset) and a simulated STEM image (lower inset) are also shown in each image.

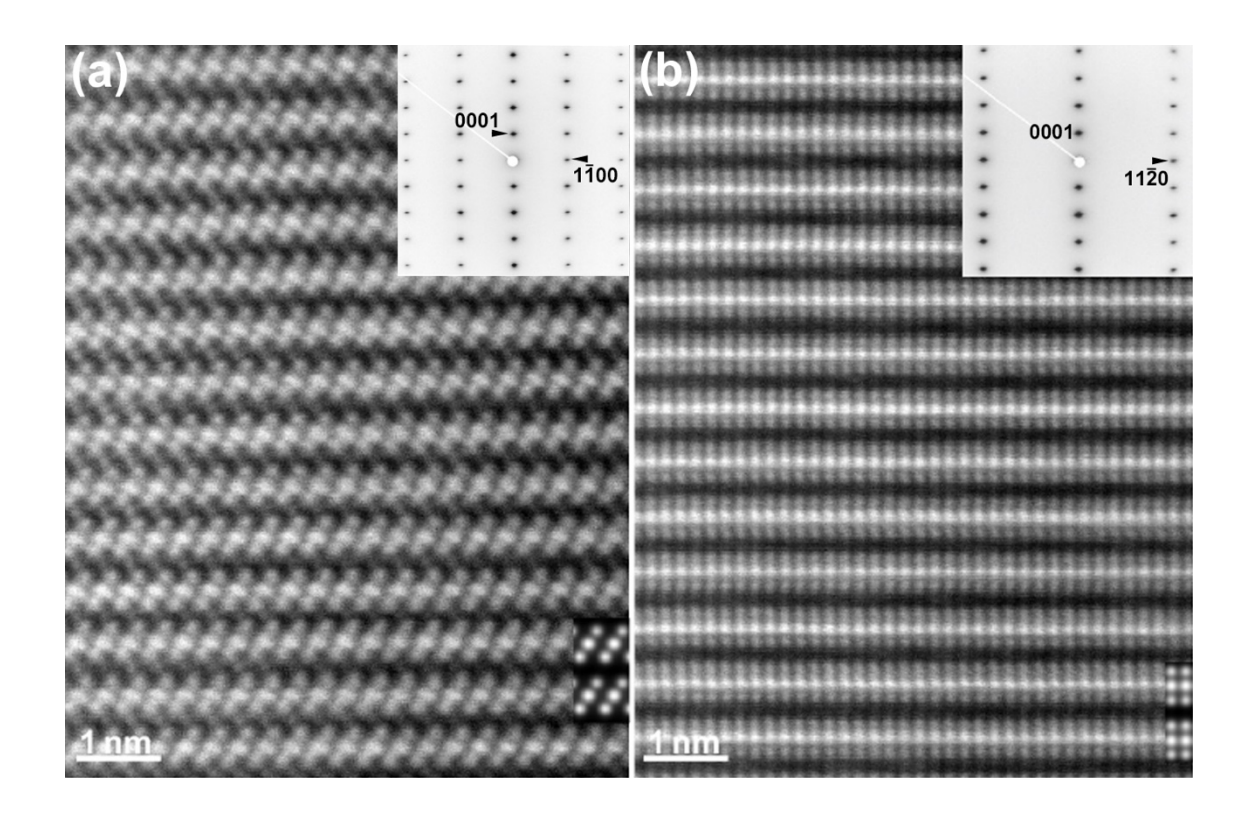


**Figure S2**. Cross-sectional HAADF-STEM images of the quenched 1T- $(Ta_{1-x}Ti_x)Se_2$  ( $x \sim 0.36$ ). (a) [11 $\overline{2}0$ ], (b) [1 $\overline{1}00$ ]. An SAED pattern (upper inset) and a simulated STEM image (lower inset) are also shown in each image.